Ferrite-SiC axially graded absorber for broadband higher-order mode damping and thermal response in a 1.5 GHz TM_{020}-mode cavity

Ziyang Xu,[1,2,*] Zhongquan Li,[1,2,*] Zhejia Xu,[1,2] Kuangkuang Ye,[1,2] Yuanli Luo,[1,2] and Xuerui Hao[3,4,†]

[1]*College of Physics, Chongqing University, No. 55 Daxuecheng South Road, Shapingba District, Chongqing 401331, P.R. China*
[2]*Laboratory for Ultrafast Transient Facility, Chongqing University, No. 174 Shazheng Street, Shapingba District, Chongqing 400044, P.R. China*
[3]*Institute of High Energy Physics, 19B Yuquan Road, Beijing 100049, P.R. China*
[4]*Spallation Neutron Source Science Center, Dongguan, Guangdong 523803, P.R. China*

(Received 10 April 2026; accepted 9 October 2026; published 28 October 2026)

The magnetic-field node of a TM_{020}-mode cavity permits compact higher-order-mode (HOM) damping, but displacement of the coupling slots can expose the absorber to appreciable accelerating-mode leakage. A ferrite-SiC absorber is investigated numerically to combine broadband damping with improved thermomechanical response in a 1.5 GHz cavity. A transmission-line formulation relates material ordering to input impedance, and coaxial full-wave calculations show that placing SiC ahead of ferrite suppresses the pronounced low-frequency absorption dip of the reverse arrangement. The concept is integrated into a radially folded, six-sector absorber, with parameter sweeps resolving the effects of material dimensions, slot height, and sector angle. For the six higher-order modes (HOMs) tabulated, external quality factors are below 150, while the aligned accelerating mode has an external quality factor of 1.20×10^7. Frequency-resolved loss maps show increasing SiC participation across the transition near 2 GHz. At the same imposed absorber load of 2.65 kW, the hybrid reduces peak temperature rise from 97.0 to 79.9 K and maximum first principal stress in ferrite from 146.0 to 78.6 MPa, reductions of 17.6% and 46.2%, respectively. These results connect electromagnetic loss redistribution to improved thermal and mechanical response and support the hybrid arrangement as a compact damping option for TM_{020}-mode cavities.

DOI: 10.1103/bp2m-nwm7

I. INTRODUCTION

Radiofrequency (rf) cavities are essential components in modern accelerator systems, providing particle acceleration, beam bunching, and energy compensation in synchrotron radiation sources, colliders, and neutron facilities [1–3]. The development of fourth-generation synchrotron light sources has intensified the challenge of coupled-bunch instabilities, which arise primarily from high beam-coupling impedances associated with higher-order modes (HOMs) excited in the accelerating cavities. Compact, high-performance higher-order-mode (HOM)-damped cavities are therefore critical for maintaining stable, high-current operation in next-generation storage rings.

The TM_{020}-mode cavity offers a useful combination of low geometric impedance R/Q, high intrinsic quality factor Q_0, and an internal magnetic-field node [4–6]. A low R/Q reduces the voltage induced by a given bunch charge and is therefore attractive for limiting transient beam loading in harmonic rf systems [7]. The magnetic-field node provides a location where an absorber can couple weakly to the accelerating mode while remaining accessible to parasitic modes with different field distributions. This spatial selectivity allows HOM damping to be integrated into the cavity body, an advantage where the available beamline length is restricted. The 1.5 GHz design considered here targets harmonic-cavity applications in a low-energy, high-current storage ring.

Practical components disturb the field symmetry on which this selectivity depends. Input couplers, tuners, and fabrication or assembly offsets can displace the magnetic nodal surface relative to the coupling slots [8,9]. Because the azimuthal magnetic field changes rapidly with radius near the node, a small displacement produces a finite field at the slot and transfers accelerating-mode energy to the absorber. For the displaced-slot quality factors considered below, a cavity-wall dissipation of 30 kW corresponds to

*These authors contributed equally to this work.
†Contact author: xrhao@ihep.ac.cn

Published by the American Physical Society under the terms of the Creative Commons Attribution 4.0 International license. Further distribution of this work must maintain attribution to the author(s) and the published article's title, journal citation, and DOI.

approximately 0.9–2.7 kW of leakage. This additional continuous load can be comparable to, or greater than, the beam-induced HOM load. Consequently, absorber design must address the heat associated with residual accelerating-mode coupling as well as the beam-coupling impedance.

Field-compensation structures and tailored coupling geometries reduce leakage at its source [9,10]. Their purpose is to preserve the accelerating-mode field pattern while maintaining access to HOMs. Material and thermal design address a complementary part of the problem: the power that reaches the load must still be dissipated and conducted to a cooled support. High-power tests of a cylindrical-shell SiC damper for the electron-ion collider demonstrate the relevance of SiC to demanding HOM loads [11], while the RHIC energy-recovery linac provides an example of ferrite-based damping [12]. These implementations establish the usefulness of both material families, but the balance between absorption, heat transport, and compact integration depends on the cavity geometry and excitation spectrum.

The present design combines ferrite and SiC along the incident-wave path instead of assigning the entire rf load to a single material. Ferrite supplies substantial magnetic dissipation in the lower-frequency range, whereas SiC provides dielectric dissipation and a higher thermal conductivity. Their arrangement also changes impedance matching and the spatial fields, so broadband performance cannot be predicted by simply adding two material loss tangents. A useful hybrid must admit energy into both segments, distribute dissipation across the relevant frequencies, and preserve thermal paths to the copper supports. These coupled requirements motivate comparison of material order before optimization of the integrated absorber geometry.

We first examine this arrangement in a coaxial test geometry and then fold the propagation path radially into the TM_{020} cavity. The numerical study combines scattering calculations, eigenmode and wakefield analyses, frequency-resolved material losses, and steady-state thermal and structural calculations. Sec. II establishes the field, power, and impedance conventions. Sec. III describes the electromagnetic and thermomechanical material inputs. Sec. IV develops the transmission-line interpretation and examines material ordering in the coaxial model. Sec. V connects full-cavity geometry selection to HOM damping, beam-induced power, and thermomechanical response. Sec. VI summarizes the design implications.

II. THEORY OF THE TM_{020}-MODE DAMPING CAVITY AND HOM ABSORBER

For an ideal cylindrical pillbox of radius R, the longitudinal electric field of the TM_{0n0} family varies as $J_0(x_{0n}r/R)$, and the azimuthal magnetic field varies as $J_1(x_{0n}r/R)$. The conducting wall imposes $J_0(x_{0n}) = 0$, giving the resonant frequency

$$f_{0n0} = \frac{cx_{0n}}{2\pi R}. \tag{1}$$

The TM_{020} mode has an interior zero of H_φ, in addition to the zero on the symmetry axis. The cavity fields in Fig. 1 illustrate the radial separation of the electric- and magnetic-energy distributions. Positioning the coupling slots near the interior magnetic node reduces their overlap with the accelerating mode [5,13]. Other monopole and dipole modes generally have different field distributions and can therefore couple to the same absorber. In a small-displacement expansion, $H_\varphi(r) \approx (dH_\varphi/dr)_{r_0}(r - r_0)$. This relation explains the sensitivity to misalignment: a geometrically small offset need not produce a small leakage load when the local field gradient is large.

Here, $x_{01} \approx 2.405$ and $x_{02} \approx 5.520$. At the same frequency, the ideal TM_{020} pillbox radius is approximately 2.3 times the TM_{010} radius. The larger radial envelope accommodates the internal damping structure; the resulting Q_0 and R/Q are determined by the full-cavity geometry. We use $(R/Q)_\parallel = |V_c|^2/(\omega U)$, where V_c is the peak effective accelerating voltage and U is the stored energy. Throughout the paper, the loaded shunt impedance is $R^*_{sh} = (R/Q)Q_L/2$. The asterisk identifies this convention. Wall dissipation is determined by the intrinsic quality factor:

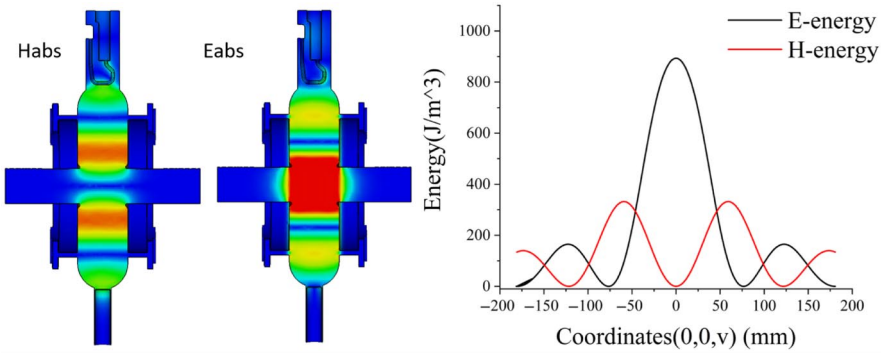


FIG. 1. Electromagnetic field distributions and energy-density profiles of the 1.5 GHz TM_{020}-mode cavity. The absorber is located near an interior radial node of H_φ.

$$P_c = |V_c|^2/[(R/Q)_{\parallel} Q_0] = \omega U/Q_0. \tag{2}$$

The reference rf condition is a cavity-wall dissipation $P_c = 30$ kW, with input-coupler coefficient $\beta_{in} = Q_0/Q_{ext,in} = 1.2$. Let $Q_{ext,leak} = \omega U/P_{leak}$ describe extraction of accelerating-mode energy into the absorbers. Since Q_0 and $Q_{ext,leak}$ refer to the same stored energy, the leakage power follows directly as

$$P_{leak} = \frac{\omega U}{Q_{ext,leak}} = P_c \frac{Q_0}{Q_{ext,leak}} \tag{3}$$

Equation (3) applies at the specified wall dissipation for any input-coupling coefficient. Forward power is a separate quantity because a fraction of the incident power can be reflected. For an on-resonance, single-input cavity without beam loading, define $b = Q_0/Q_{ext,leak}$; the corresponding balance is $P_{fwd} = P_c(1 + \beta_{in} + b)^2/(4\beta_{in})$. Matching to the combined wall and absorber load occurs at $\beta_{in} = 1 + b$. Beam loading and detuning modify the forward-power requirement, while the relation between P_c and P_{leak} in Eq. (3) follows from the loss definitions. With $Q_0 \approx 3 \times 10^4$ and $Q_{ext,leak}$ between 3.3×10^5 and 1.0×10^6, the displaced-slot cases give

$$P_{leak} \approx 30\ \text{kW} \times [3 \times 10^4/(3.3 \times 10^5\ \text{to}\ 1.0 \times 10^6)] \approx 0.9\text{–}2.7\ \text{kW}. \tag{4}$$

By comparison, the aligned configuration in Table II has $Q_0 = 36,100$ and $Q_{ext,leak} = 1.20 \times 10^7$, corresponding to 90.3 W at the same wall dissipation. The difference between aligned and displaced configurations shows why low nominal leakage alone is insufficient to size the absorber cooling system. The 1.50 kW leakage contribution used in the thermal comparison represents a displaced-geometry load within the range of Eq. (4). It provides a common additional heat load for comparing the two absorber materials.

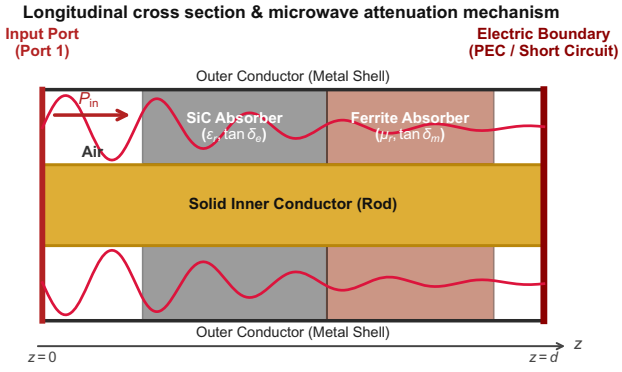


FIG. 2. Longitudinal schematic of the coaxial absorber and microwave attenuation. Port 1 at $z = 0$ launches power P_{in} into the air section followed by SiC and ferrite between the solid inner conductor and outer metal shell. The back end at $z = d$ is a perfect-electric-conductor (PEC) short circuit. The material labels indicate dielectric and magnetic loss parameters, and the red curves schematically illustrate attenuation. Port 1 is the scattering reference port, distinct from the cavity rf input coupler.

Using peak-amplitude phasors with time dependence $e^{j\omega t}$, write $\epsilon_r = \epsilon_r' - j\epsilon_r''$ and $\mu_r = \mu_r' - j\mu_r''$. For linear isotropic media without impressed volume sources, the electric- and magnetic-field equations are

$$\nabla \times [\mu_r^{-1} \nabla \times E] - k_{vac}^2 \epsilon_r E = 0, \qquad k_{vac} = \omega/c \tag{5}$$

$$\nabla \times [\epsilon_r^{-1} \nabla \times H] - k_{vac}^2 \mu_r H = 0. \tag{6}$$

Absorption in the coaxial model is evaluated at port 1, upstream of the material segments (Fig. 2). The solid inner conductor and outer shell guide the incident wave through an air section, SiC, and ferrite to a conducting short circuit. For a single propagating incident mode, negligible conductor loss, and no transmitted channel, the fraction of incident power dissipated in the absorber is $\eta = 1 - |S_{11}|^2$. The more general definition is $\eta = P_{abs}/P_{in}$, where P_{abs} is the volume-integrated absorber loss. If additional propagating modes or conducting-wall losses are appreciable, their powers enter the port balance explicitly. The scattering port defines the absorber excitation independently of the cavity input coupler.

The incident and reflected fields carry a single electromagnetic energy flux. Within the material, irreversible conversion of that energy to heat occurs through dielectric and magnetic loss. Applying the time-averaged Poynting theorem to an absorber volume V, with outward unit normal n, gives

$$P_{abs} = -\frac{1}{2}\text{Re} \oint_{\partial V} (E \times H^*) \cdot n dA = \int_V (p_e + p_m) dV = P_e + P_m \tag{7}$$

$$p_m = (\omega \mu_0/2)\mu_r'' |H|^2, \qquad P_m = \int_V p_m dV \tag{8}$$

$$p_e = (\omega \epsilon_0/2)\epsilon_r'' |E|^2, \qquad P_e = \int_V p_e dV. \tag{9}$$

The local quantities p_e and p_m are power densities in W/m^3; their volume integrals are powers in W. Conductivity is included in ϵ_r'' in Eq. (9); if specified separately, its contribution is $\sigma|E|^2/2$ and is counted once. The power deposited in material i is $P_i = \int_{V_i} (p_e + p_m) dV$, for i = ferrite or SiC. This material integral includes both loss mechanisms and provides the link from the rf calculation to the thermal source. The distinction is useful for a hybrid absorber: magnetic dissipation may dominate in ferrite and dielectric dissipation in SiC, but their relative

contributions also depend on the fields established by the complete geometry.

III. PHYSICAL MECHANISMS OF ELECTROMAGNETIC ABSORPTION AND MATERIAL SELECTION

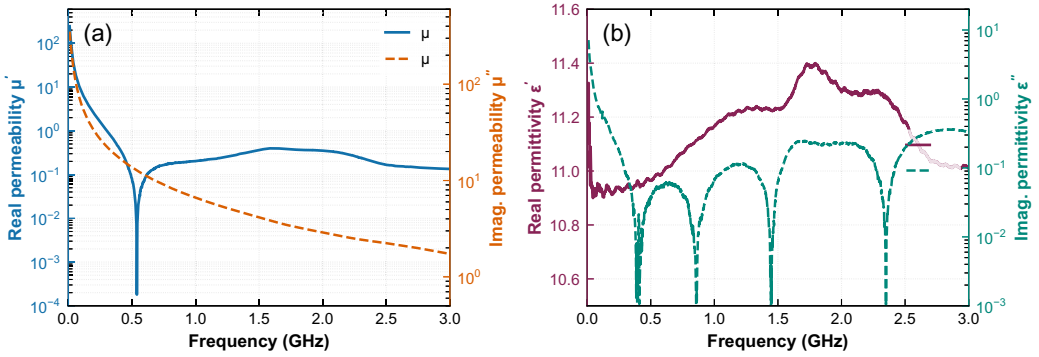
An HOM absorber must combine a suitable complex electromagnetic response with a practical route for heat removal. Figure 3 shows the frequency-dependent relative permeability and permittivity used to characterize the ferrite and SiC. Their real parts influence propagation and impedance, while their imaginary parts determine local dissipation through Eqs. (8) and (9). The material choice is therefore governed by both field penetration and loss, rather than by the largest imaginary parameter alone. Table I gives the thermal and elastic inputs used in the comparative model, together with the ferrite strength measurements relevant to interpreting the calculated stresses.

SiC ceramics dissipate rf energy predominantly through their dielectric response. In polycrystalline SiC, electrically conducting grains and more resistive grain boundaries can produce interfacial polarization and relaxation [14]. The associated phase lag between electric field and polarization contributes to ϵ_r'', alongside conduction. A single-relaxation representation illustrates these contributions:

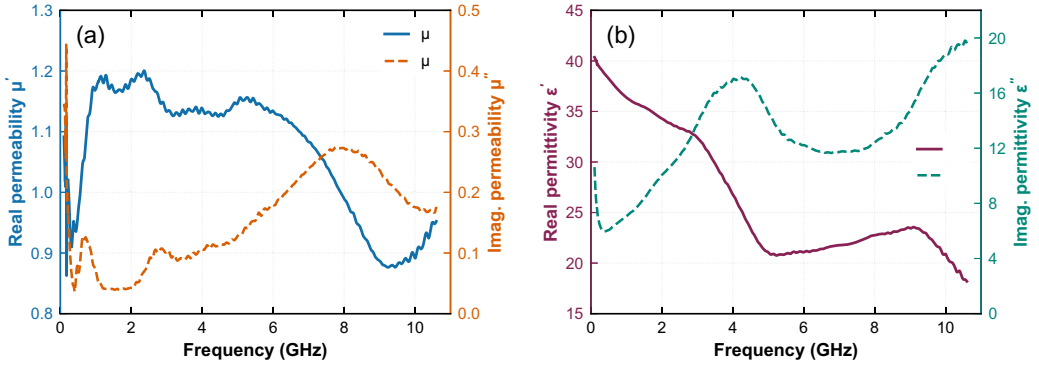
$$\epsilon_r(\omega) = \epsilon_\infty + (\epsilon_s - \epsilon_\infty)/(1 + j\omega\tau) + \sigma/(j\omega\epsilon_0) \quad (10)$$

Here, ϵ_s and ϵ_∞ are the static and high-frequency relative permittivities, τ is the relaxation time, σ is conductivity, and ϵ_0 is vacuum permittivity. Equation (10) describes a relaxation mechanism; the frequency-dependent spectrum in Fig. 3 supplies the material response for this study. In the plotted SiC data, ϵ_r'' falls from approximately 40 at the low-frequency end to about 21 near 5 GHz. The imaginary part grows through much of the 1–4 GHz range, reaching about 17 near 4 GHz, and then varies nonmonotonically at higher frequencies. Over most of this range, μ_r' remains near unity and μ_r'' is much smaller than the ferrite value. These trends favor dielectric absorption in SiC while leaving a role for ferrite at lower frequencies.

The large real permittivity of SiC also alters wavelength, impedance, and field penetration. Strong dielectric loss is useful only when a sufficient field reaches the ceramic; a poorly matched entrance can reflect power before it is dissipated. The leading SiC segment consequently acts as both a lossy region and an impedance-transforming



(a) Ferrite: (a) relative permeability; (b) relative permittivity



(b) SiC: (a) relative permeability; (b) relative permittivity

FIG. 3. Frequency-dependent complex relative permeability and permittivity of ferrite (upper pair) and SiC (lower pair). For each material, panel (a) shows μ' and μ'' and panel (b) shows ϵ' and ϵ''. All constitutive parameters are dimensionless. Left and right axes have independent scales; the frequency ranges are 0–3 GHz for ferrite and approximately 0–11 GHz for SiC.

TABLE I. Thermal and elastic model inputs and ferrite mechanical test results [15,17,18]. Strength entries refer to distinct loading configurations; a dash denotes a value not evaluated in this comparison.

Property	Ferrite	SiC
Thermal conductivity k, $\mathrm{W/(m \cdot K)}$	3.2	150
Specific heat c_p, $\mathrm{J/(kg \cdot K)}$	540	800
Density ρ, $\mathrm{g/cm^3}$	4.9	3.2
Young's / tensile modulus E, GPa	110	410
Poisson ratio ν, dimensionless	0.23	0.21
Thermal expansion α, 10^{-6} $\mathrm{K^{-1}}$	9.61	4.4
Tensile strength, MPa	18.3	270
Tensile yield strength, MPa	No yielding observed	…
Three-point flexural strength, MPa	99.6	…
Compressive strength, MPa	274	…

section. Its high thermal conductivity, 150 $\mathrm{W/(m \cdot K)}$ in Table I, provides a further incentive to deposit part of the rf power in this material. SiC-based HOM loads illustrate this combination of dielectric absorption and heat-transport capability [11,14,15].

Ferrite supplies a strongly dispersive magnetic response. In Fig. 3, μ_r'' reaches values of order 10^2 at the low-frequency end and decreases as frequency increases; a finite-frequency maximum is not resolved within this displayed interval. Substantial magnetic loss persists over the lower-frequency part of the HOM spectrum. The real permeability is also dispersive, while the real permittivity stays close to 11 across the plotted band. Magnetic and dielectric responses therefore both enter the field solution, even where magnetic dissipation dominates. The trade-off between high initial permeability and high characteristic magnetic-response frequency is expressed schematically by a Snoek-type relation [16],

$$(\mu_i - 1) f_r \propto \gamma M_s, \tag{11}$$

where μ_i is initial permeability, f_r is a characteristic magnetic-response frequency, γ is the gyromagnetic ratio, and M_s is saturation magnetization. The proportionality depends on the material model and unit convention. The relation explains why increasing low-frequency permeability does not provide an unrestricted extension of the useful magnetic response to higher frequencies. It does not imply an abrupt disappearance of device absorption at 2 GHz: ferrite retains a finite loss, and the total absorbed power depends on the local field and propagation length. Combining it with SiC broadens the available dissipation mechanisms while reducing reliance on ferrite for the entire heat load.

The thermal conductivity contrast between the two materials is approximately 47:1, whereas their elastic and expansion properties differ in another direction: SiC is stiffer, but ferrite has the larger thermal expansion coefficient. Consequently, a lower temperature rise does not uniquely determine the stress in the bonded assembly. Heat-source distribution, deformation constraints, and material mismatch must be considered together. Specific heat and density are included in Table I as material properties, although the steady-state temperature comparison is governed by conductivity and the thermal boundary conditions rather than heat capacity.

Report STD-20200714-039 N gives ferrite tensile strength 18.3 MPa, three-point flexural strength 99.6 MPa, compressive strength 274 MPa, tensile modulus 110 GPa, and Poisson ratio 0.23 [17]. No yielding was observed in tension. The measurements were made at 21–22 °C and 53%–54% relative humidity. These distinct test results motivate a brittle-material interpretation of the stress field rather than a ductile yield criterion. Their relation to the localized thermal stresses is examined in Sec. V D, together with the comparison between pure-ferrite and hybrid assemblies.

IV. TRANSMISSION-LINE INTERPRETATION AND COAXIAL NUMERICAL STUDY

The coaxial study separates two questions: how the order of the materials changes the impedance seen by the incident wave, and how the available segment lengths determine attenuation over frequency. A distributed transmission-line model provides the physical interpretation of these effects. Full-wave simulations in CST Microwave Studio then evaluate the actual coaxial geometry, including field distributions and reflections at material interfaces. This progression establishes the design rationale before introducing the folded geometry of the cavity absorber.

A. Frequency-complementary broadband matching

Each uniform segment is represented by a per-unit-length series impedance $z = R + j\omega L$ and shunt admittance $y = G + j\omega C$. Magnetic loss contributes to the effective series resistance, while dielectric loss contributes to shunt conductance. Both materials can have nonzero series and shunt losses. The propagation constant $\gamma = \sqrt{zy}$ and characteristic impedance $Z = \sqrt{z/y}$ govern the relation between voltage and current. These are modal quantities for the specified cross section, including its material filling. The cascade in Fig. 4 therefore accounts for absorption and mismatch within the same network description. For a segment i of length l_i, the transfer matrix is

$$\begin{pmatrix} A_i & B_i \\ C_i & D_i \end{pmatrix} = \begin{pmatrix} \cos h(\gamma_i l_i) & Z_i \sin h(\gamma_i l_i) \\ \frac{1}{Z_i} \sin h(\gamma_i l_i) & \cos h(\gamma_i l_i) \end{pmatrix} \tag{12}$$

For incidence from the SiC side, the ordered cascade is $M_T = M_{air} \cdot M_{SiC} \cdot M_{ferrite}$. Its entries give

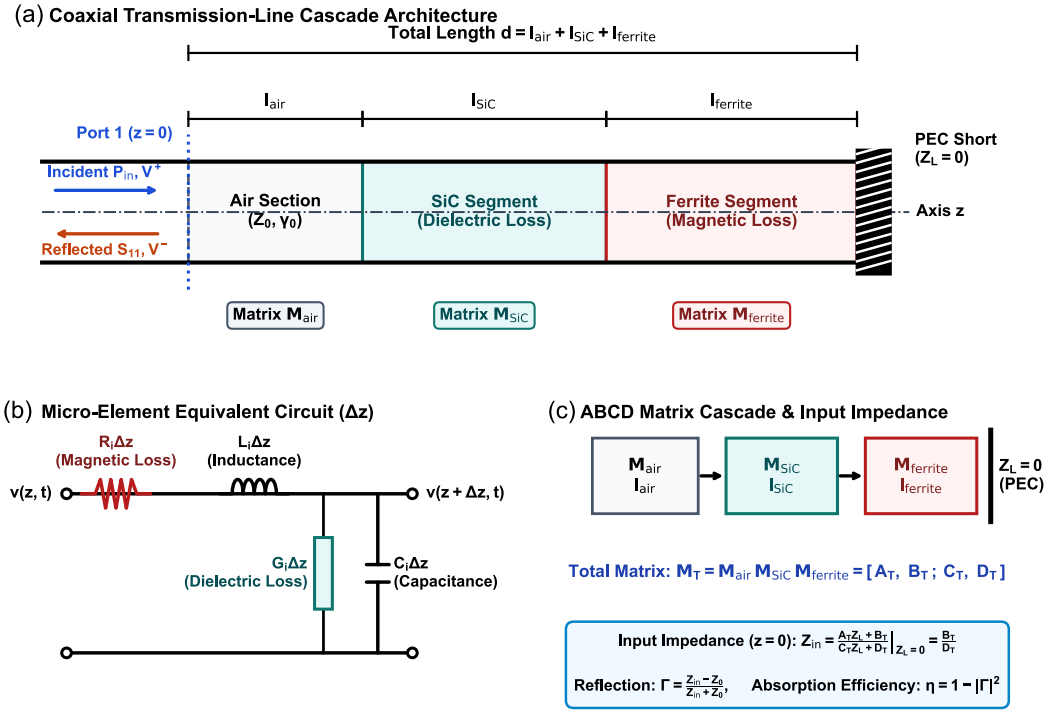


FIG. 4. Reduced-order transmission-line cascade and microelement equivalent circuit. (a) Coaxial transmission-line cascade architecture with air, SiC, and ferrite sections terminated by a PEC short circuit. (b) Equivalent circuit of a per-unit-length microelement Δz including series resistance $R_i\Delta z$, series inductance $L_i\Delta z$, shunt conductance $G_i\Delta z$, and shunt capacitance $C_i\Delta z$. (c) ABCD matrix cascade representation and input impedance expression.

$Z_{\mathrm{in}} = (A_{\mathrm{T}}Z_{\mathrm{L}} + B_{\mathrm{T}})/(C_{\mathrm{T}}Z_{\mathrm{L}} + D_{\mathrm{T}})$, reducing to $B_{\mathrm{T}}/D_{\mathrm{T}}$ at the short circuit $Z_{\mathrm{L}} = 0$. Swapping the materials changes the matrix order. For two segments, for example, the A entry contains $(Z_1/Z_2)\sin h(\gamma_1 l_1)\sin h(\gamma_2 l_2)$; reversing them replaces this impedance ratio by Z_2/Z_1. Thus, the same constituent materials and lengths can produce different input impedances. The resulting reflection coefficient at a reference impedance Z_0 is

$$\Gamma = (Z_{\mathrm{in}} - Z_0)/(Z_{\mathrm{in}} + Z_0), \qquad \eta = 1 - |\Gamma|^2. \tag{13}$$

Efficient broadband absorption requires both a small entrance reflection and sufficient dissipation during propagation. Increasing material loss can improve attenuation while simultaneously worsening mismatch, so neither property alone determines η. A SiC-first arrangement changes the field reaching the ferrite and the phase of the wave reflected by the short circuit. At lower frequencies, ferrite supplies the strong magnetic loss needed to attenuate energy that penetrates the leading section. At higher frequencies, dielectric loss in SiC provides an additional dissipation path. The resulting division is gradual and geometry-dependent; the two sections remain parts of one coupled electromagnetic system.

The attenuation requirement can be estimated separately from entrance matching. Let α_{fer} be the ferrite field-amplitude attenuation coefficient. A wave entering a ferrite length L_{fer}, reflecting from the conducting back wall, and returning through the segment has a surviving power fraction $e^{-4\alpha_{\mathrm{fer}}L_{\mathrm{fer}}}$. Neglecting entrance reflection and interface multiple reflections, a target dissipated fraction η_{target} gives

$$\begin{aligned} e^{(-4\alpha_{\mathrm{fer}}L_{\mathrm{fer}})} &\le 1 - \eta_{\mathrm{target}}, \\ L_{\mathrm{fer,min}} &\ge -\ln(1 - \eta_{\mathrm{target}})/(4\alpha_{\mathrm{fer}}). \end{aligned} \tag{14}$$

For the illustrative attenuation input $\alpha_{\mathrm{fer}} = 43.6$ Np/m at 1.0 GHz and $\eta_{\mathrm{target}} = 0.9$,

$$L_{\mathrm{fer,min}} = -\ln(0.1)/(4 \times 43.6) = 13.2\ \mathrm{mm}. \tag{15}$$

A 14 mm ferrite length gives approximately 91.3% round-trip dissipation under this approximation. The estimate establishes a useful attenuation length scale for energy already admitted into the ferrite. The complete absorber must also satisfy the matching condition through Eq. (13), which depends on real and imaginary material parameters and the geometry. In particular, a small ϵ_{r}'' does not make the SiC impedance equal to that of the air-filled line. The full-wave parameter study therefore examines the entrance section and rear loss section together instead of assigning a broadband optimum from the attenuation length alone.

B. Coaxial numerical comparison

Figure 5 compares SiC + ferrite, ferrite + SiC, and vacuum + ferrite in the coaxial geometry. The names specify the sequence viewed from port 1 toward the short circuit. The geometry inset defines the two axial dimensions L_0 and L_1; the sweep parameter is their ratio $a = L_0/L_1$. The overview uses $a = 0.5$, and the three grouped panels cover $a = 0.1, 0.3, 0.5, 0.7,$ and 0.9. Absorption is plotted as $A(f) = 100\eta$ in percent. The 90% horizontal line serves as a common reference for comparing bandwidth and the depth of absorption minima.

At $a = 0.5$, the SiC-first arrangement provides the most uniform high-frequency response of the three overview curves: absorption rises from approximately 76% at low frequency to about 90% near 1.5 GHz and remains above that level across most of the upper band. The ferrite-first arrangement has a pronounced minimum near 0.85 GHz, where absorption falls to approximately 47%, before recovering. The vacuum-first arrangement reaches high efficiencies in separate frequency regions but develops a broad minimum near 2.5–3 GHz. These differences show that material order controls the location and severity of mismatch features, not simply the total amount of lossy material encountered by the wave.

The SiC-first sweep in Fig. 6(a) shows that increasing a from 0.1 toward 0.7–0.9 substantially improves the lower-frequency response. At small a, the low-frequency efficiency is only about 55%–65%, whereas the larger-ratio curves approach the 90% reference over a much wider interval. Above approximately 2 GHz, the curves lie closer together, with crossings and shallow minima that reflect the frequency dependence of the transformed input impedance. Thus, the ratio strongly controls low-frequency matching, while the combination of both loss mechanisms sustains a relatively broad upper-frequency response. The parameter a is an axial-dimension ratio, not a material volume fraction.

Reversing the materials gives a different dependence on a Fig. 6(b). Ratios of 0.1 and 0.3 produce deep minima near 0.7–0.8 GHz, with efficiencies around 20%, while larger ratios weaken or shift these minima. A substantial recovery above about 2 GHz shows that ferrite at the entrance does not block all high-frequency absorption. Rather, the reverse arrangement is more sensitive to low-frequency matching in the cases examined. This behavior is consistent with the noncommuting transfer matrices: changing the first segment modifies both the impedance transformation and the field amplitude available to the second segment.

The vacuum-first cases in Fig. 6(c) isolate the response of a lossless entrance section coupled to the rear ferrite. Their broad oscillations and crossing curves show that phase advance and reflection alone can produce high absorption at selected frequencies. However, the largest-ratio case develops an extended high-frequency depression, reaching roughly 20% near 4.5 GHz. Vacuum replacement therefore has a strongly frequency-dependent effect, rather than a constant reduction in efficiency. Taken with the SiC-first results, this comparison supports using a lossy entrance section to obtain a more even response across the band. Material-resolved losses in the integrated

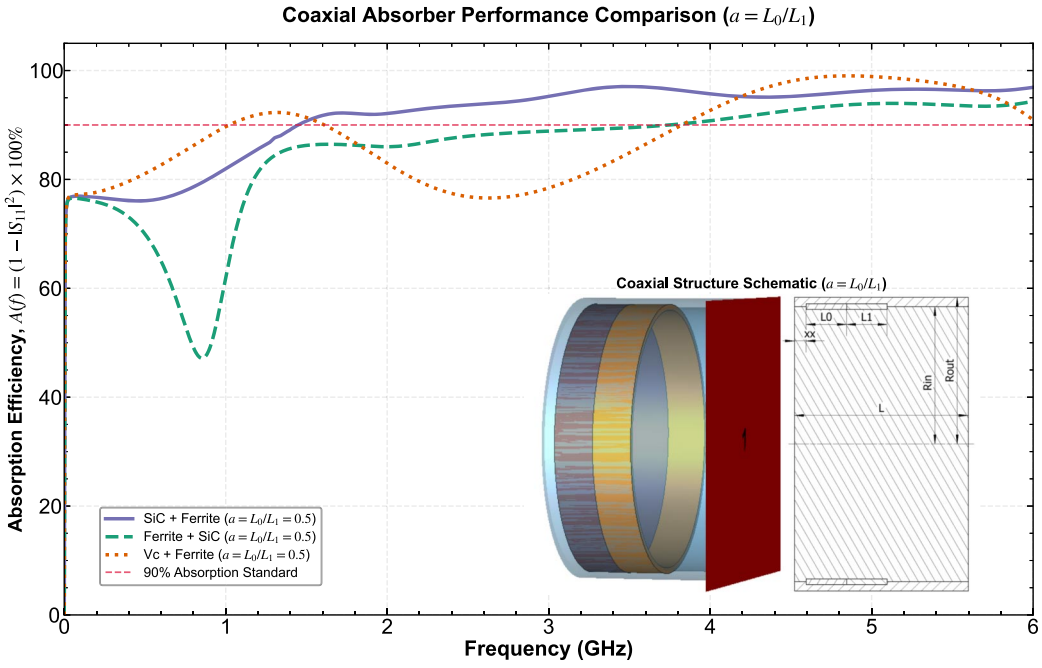


FIG. 5. Overview and coaxial geometry. The overview compares SiC + ferrite, ferrite + SiC, and vacuum (Vc) + ferrite at $a = L_0/L_1 = 0.5$ and includes the geometry inset.

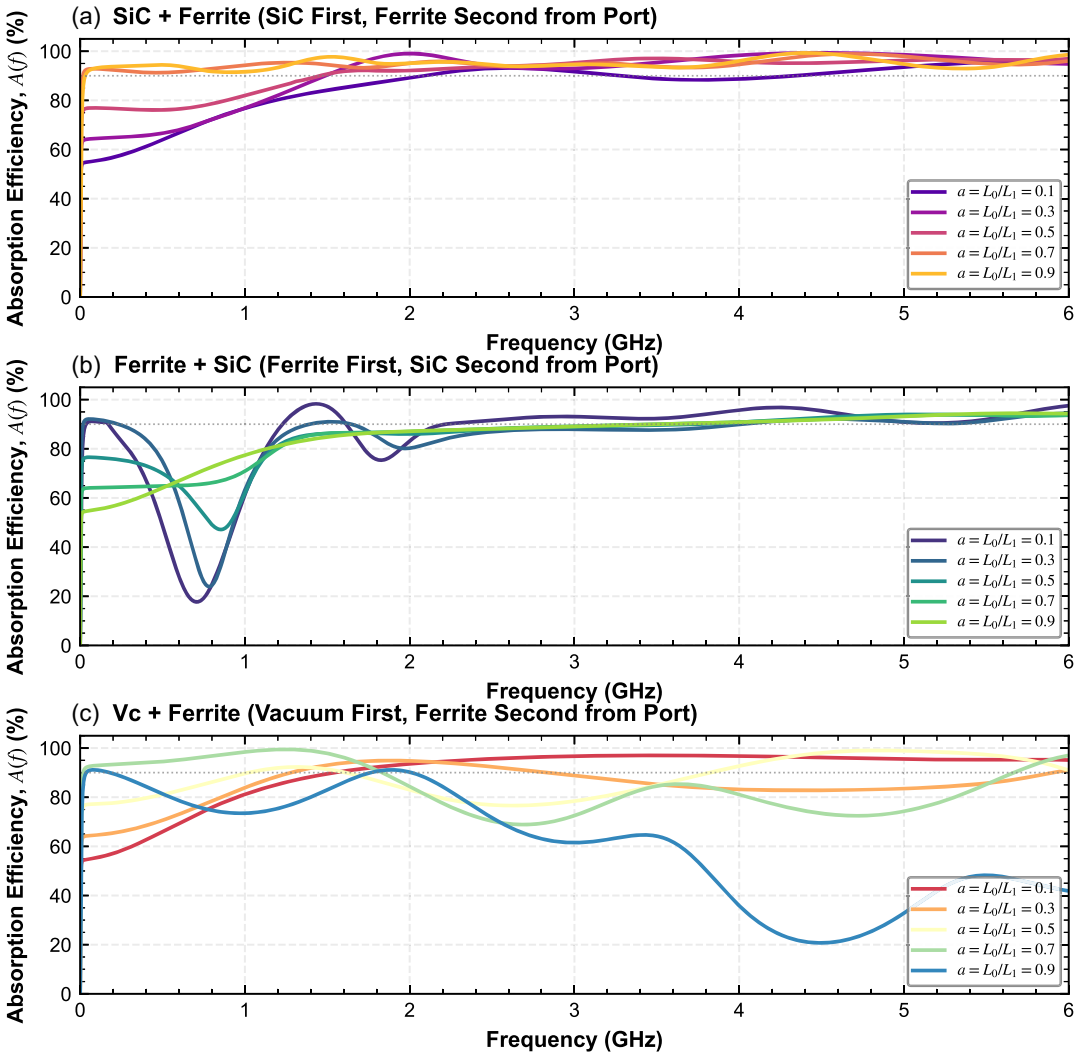


FIG. 6. Coaxial absorber response. The grouped panels show (a) SiC first and ferrite second, (b) ferrite first and SiC second, and (c) vacuum first and ferrite second, for $a = 0.1$–0.9. Material order is defined from the incident port. $A(f) = 100\eta$ is absorption in percent; horizontal lines mark 90%.

absorber, examined in Sec. V C, establish where the admitted power is dissipated.

V. FULL-CAVITY INTEGRATION AND PERFORMANCE EVALUATION

A. Absorber topology and full-wave design selection

The integrated cavity uses a radial fold of the coaxial absorption path to accommodate the load within the cavity's outer envelope (Figs. 7 and 8). Rf energy couples through slots near the TM_{020} magnetic node and enters the folded material region without requiring a separate axial beamline absorber. The assembly is divided azimuthally into six sectors, allowing individual ceramic pieces, and their copper supports to be handled and mounted separately. The single-layer configuration, labeled "oneway,"

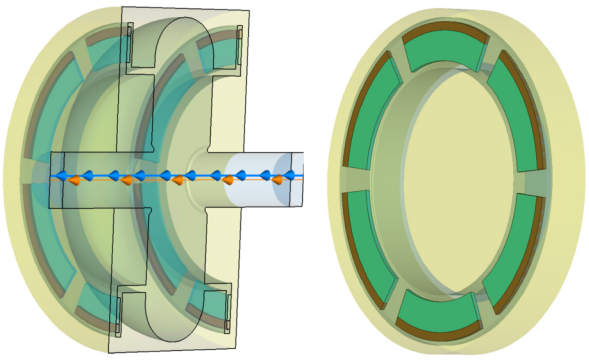


FIG. 7. Integrated TM_{020}-mode cavity and hybrid absorber. Brown denotes ferrite, and cyan denotes SiC.

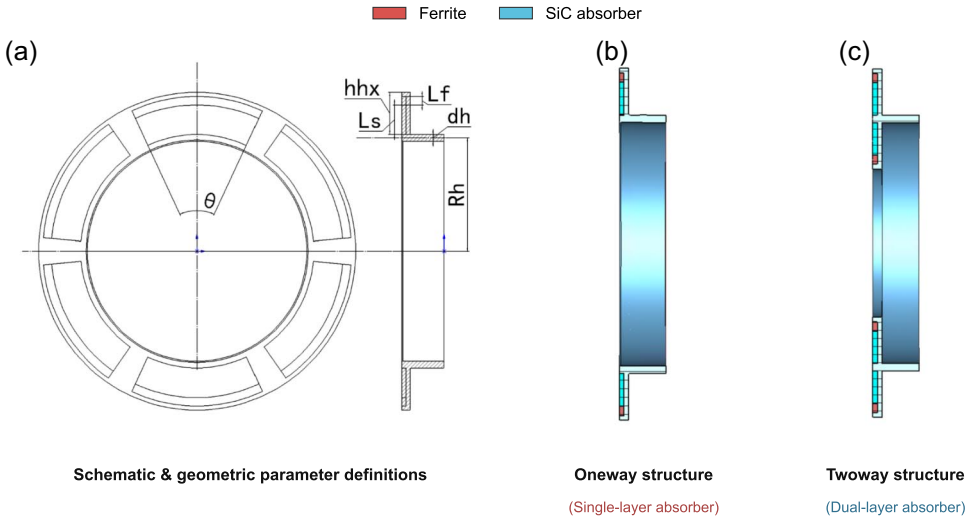


FIG. 8. Folded absorber geometry. (a) Schematic and geometric parameter definitions (where θ is the half-angle of each sector, giving a total angular span of 2θ). (b) Single-layer ("oneway") and (c) dual-layer ("twoway") configurations. Red denotes ferrite and cyan denotes SiC. Lf and Ls are radial material dimensions; hhx is slot height, dh is the coupling-slot width (the gap between inner and outer coaxial conductors), R_{h} is coaxial center radius, and θ is sector half-angle.

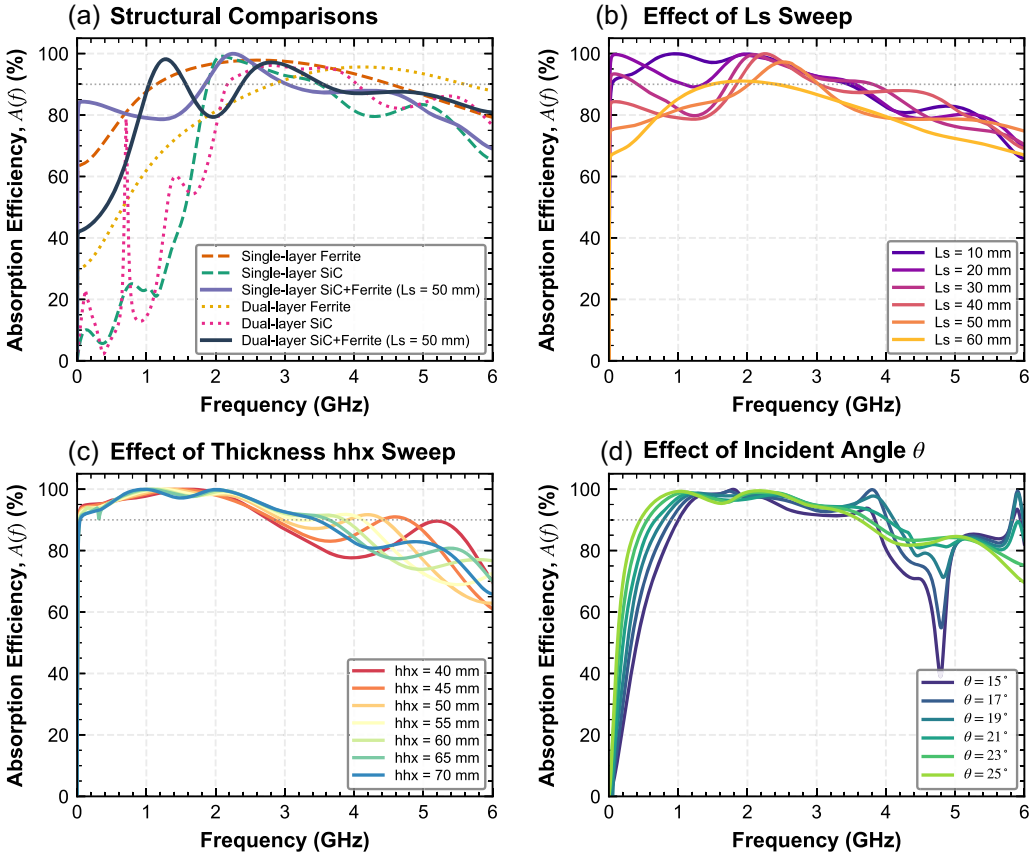


FIG. 9. Absorption efficiency of the integrated absorber structure under different parameter sweeps. (a) Comparison of single-layer and dual-layer configurations (with $Ls = 60$ mm, $Lf = 10$ mm, and $\theta = 30°$). (b) Sweep of Ls from 10 to 60 mm at fixed total height $hhx = 70$ mm and $\theta = 30°$, essentially evaluating the material length ratio Ls/Lf. (c) Sweep of total slot height hhx from 40 to 70 mm for fixed $Lf = 10$ mm and $\theta = 30°$, representing a direct variation of SiC length Ls. In panels (b),(c), $\theta = 30°$ corresponds to six contiguous sectors forming a closed 360° ring. (d) Sweep of sector half-angle θ from 15° to 30° for fixed $Lf = 10$ mm and $Ls = 60$ mm. Efficiency η is expressed in percent; dotted horizontal lines represent the 90% reference.

contains one folded absorber layer; the dual-layer "two-way" configuration contains two. These labels describe the mechanical topology. In the hybrid configuration, SiC precedes ferrite along the incident path into the material region.

The geometric variables separate material allocation from coupling-aperture design. Lf and Ls are the radial dimensions of the ferrite and SiC segments, hhx is the total slot height, dh is the gap between inner and outer coaxial conductors (the coupling-slot width), R_{h} is the coaxial center radius, and θ is the sector half-angle (giving a total sector angle of 2θ). In Fig. 9, the parameter sweeps systematically isolate these contributions under defined constraints. For the Ls sweep in Fig. 9(b), the total slot height is fixed at $hhx = 70$ mm, so varying Ls from 10 to 60 mm corresponds to a complementary variation of Lf from 60 to 10 mm; this sweep essentially evaluates the material length ratio Ls/Lf. Conversely, the hhx sweep in Fig. 9(c) maintains a constant ferrite thickness $Lf = 10$ mm, meaning that increasing hhx from 40 to 70 mm corresponds directly to varying the SiC segment length Ls. In both Figs. 9(b) and 9(c), the sector half-angle is set to $\theta = 30°$ (full angle 60°), such that the six sectors are contiguous and form a continuous 360° annular absorber ring. Finally, the sector-angle sweep in Fig. 9(d) varies θ from 15° to 30° for the fixed baseline material allocation of $Lf = 10$ mm and $Ls = 60$ mm ($hhx = 70$ mm).

Figure 9(a) compares the spectral absorption of single-layer ("oneway") and dual-layer ("twoway") topologies for ferrite, SiC, and hybrid materials. Adding a second layer does not produce a uniform improvement across the spectrum: while the dual-layer hybrid reaches high absorption near 1.2 GHz, it exhibits a more pronounced neighboring minimum around 2 GHz. Pure-SiC configurations show deep low-frequency depressions below 1.5 GHz due to weak low-frequency magnetic loss, whereas ferrite-containing configurations couple effectively in this range. The single-layer hybrid provides a favorable compromise by suppressing deep absorption gaps and maintaining high broadband efficiency in a simpler mechanical structure.

The Ls sweep in Fig. 9(b) illustrates how altering the material allocation ratio Ls/Lf at fixed total length $hhx = 70$ mm and $\theta = 30°$ redistributes dissipation between magnetic and dielectric mechanisms. Increasing Ls (and thus increasing Ls/Lf from 10/60 to 60/10) transforms the entrance matching and internal field penetration. At small Ls (e.g., $Ls = 10$–20 mm, where ferrite dominates the slot length), absorption is relatively high at low frequencies (< 1.5 GHz) but exhibits notable depressions above 2 GHz. As Ls increases to 50–60 mm ($Lf = 20$–10 mm), the SiC segment provides enhanced impedance transformation and dielectric loss, suppressing high-frequency absorption drops and sustaining a broad, high-efficiency band (> 90%) across 2–6 GHz. This establishes that a large SiC-to-ferrite length ratio $Ls/Lf = 60/10$ (6:1) optimizes broadband matching while confining the ferrite to a compact 10 mm end section.

Varying the total slot height hhx from 40 to 70 mm while fixing $Lf = 10$ mm and $\theta = 30°$ [Fig. 9(c)] directly tests the effect of extending the SiC segment length Ls from 30 to 60 mm. The curves show that increasing hhx (and thus increasing Ls) monotonically improves low-frequency matching below 2 GHz without compromising high-frequency absorption. For $hhx = 40$ mm ($Ls = 30$ mm), absorption drops below 80% around 1.2 GHz due to insufficient dielectric attenuation length; expanding hhx to 70 mm ($Ls = 60$ mm) lifts the low-frequency absorption above 90% across almost the entire band. This indicates that a minimum SiC length of $Ls = 60$ mm is required for complete wave attenuation before reaching the shorted ferrite end.

The sector-angle sweep in Fig. 9(d) evaluates azimuthal coverage for the baseline dimensions $Lf = 10$ mm and $Ls = 60$ mm ($hhx = 70$ mm). Increasing the half-angle θ from 15° to 30° progressively closes the azimuthal gaps between sectors. Smaller half-angles ($\theta = 15°$–$20°$, total coverage 180°–240°) create severe absorption dips around 4.7 GHz due to field leakage through the unshielded azimuthal gaps. As θ approaches 25°–30° (total coverage 300°–360°), the azimuthal field coupling becomes nearly uniform, eliminating the high-frequency dip and providing robust absorption above 90%. When $\theta = 30°$, the six sectors join into a continuous 360° ring, achieving maximum coupling efficiency. However, considering practical fabrication and assembly clearance for mounting individual cooling plates, a sector angle of $\theta = 23°$ (giving a total span of 46° per sector with small intersector assembly gaps) is selected for the reference design, retaining near-optimal rf absorption while accommodating mechanical support constraints.

The reference single-layer assembly is thus established with $Ls = 60$ mm, $Lf = 10$ mm, $hhx = 70$ mm, and $\theta = 23°$ (with $\theta = 30°$ representing the contiguous ring limit). This configuration achieves high broadband efficiency (> 90%) over 0.5–6 GHz by pairing a leading 60 mm SiC impedance-matching section with a 10 mm ferrite magnetic-loss backing, combined with a 23° sector coverage that balances electromagnetic performance against mechanical assembly requirements.

B. Wakefield analysis and HOM impedance

The cavity-absorber system is evaluated with two complementary full-wave calculations. Eigenmode analysis in CST resolves selected resonances and their wall and external losses, while wakefield analysis follows the transient response to a relativistic bunch and obtains broadband impedances by Fourier transformation. The eigenmode results identify which modes remain weakly

TABLE II. Selected modal parameters of the integrated cavity-absorber system. The convention is $R^*_{sh} = (R/Q)Q_L/2$. R/Q and R^*_{sh} are in Ω and kΩ for monopoles, and Ω/m and kΩ/m for dipoles. TM_{020} is the accelerating mode.

Mode	f (GHz)	Q_0	Q_{ext}	R/Q	Rsh∗
TM020	1.499	36100	1.20×10^7	55.3	995.171
TM010	0.656	24736.2	25.09	125.8	0.53
TM011	2.397	27369.65	110	7.94	0.876
TM021	3.060	30492.73	148	8.51	0.776
TM110	1.026	29676.24	19	1004	9.57
TM111	1.872	36588.28	43.5	919	19.96
TM120	2.564	25097.5	143	780	55.78

or strongly coupled to the absorber. The wakefield spectra show the combined response, including features outside the selected modal set, and permit comparison with the ring's longitudinal and transverse instability thresholds.

The common shunt-impedance convention is $R^*_{sh} = (R/Q)Q_L/2$, with $Q_L^{-1} = Q_0^{-1} + Q_{ext}^{-1}$ for the passive cavity-absorber model. Here, Q_{ext} describes external damping in that model and excludes the driven input-coupler loading. For longitudinal modes, $(R/Q)_\parallel = |V_\parallel|^2/(\omega U)$, so $R^*_{sh,\parallel} = |V_\parallel|^2/(2P_{loss,L})$, where $P_{loss,L} = \omega U/Q_L$. The asterisk is a convention label, not complex conjugation. An isolated longitudinal mode has Re $Z_\parallel(\omega_m) = R^*_{sh,\parallel}$ and Re $Z_\parallel(\omega) = R^*_{sh,\parallel}/[1 + Q_L^2(\omega/\omega_m - \omega_m/\omega)^2]$. This expression relates the modal impedance to the resonant line shape used in the power calculation.

Table II lists the accelerating mode and six selected HOMs between 0.656 and 3.060 GHz. The longitudinal HOM impedances in this set reach 0.876 kΩ, and the dipole entries reach 55.78 kΩ/m. Monopole R/Q and R^*_{sh} have units Ω and kΩ; the transverse entries use the per-length normalization shown in the table. The accelerating-mode value is 995.171 kΩ with $Q_L = 35,991.7$. Its much larger impedance is consistent with preserving a useful accelerating resonance while extracting energy from the parasitic modes.

All six HOMs in Table II have $Q_{ext} < 150$, whereas their wall quality factors are of order 10^4. Their loaded quality factors are therefore governed primarily by energy extraction into the damping system. The lowest dipole mode TM_{110} has $Q_{ext} = 19$, and TM_{111} has $Q_{ext} = 43.5$, indicating particularly strong damping for these resonances. In contrast, the aligned accelerating mode has $Q_{ext,leak} = 1.20 \times 10^7$, far above its Q_0. The separation between these loss rates demonstrates the modal selectivity of placing the coupling structure near the accelerating-mode magnetic node. Broadband behavior is assessed separately through Fig. 10.

The longitudinal spectra in Fig. 10(a) show why the ferrite segment remains useful even when SiC is included for heat transport. Relative to pure SiC, the ferrite-containing absorbers reduce the strong low-frequency structure below 1 GHz. At higher frequencies, the three spectra lie closer together over substantial intervals, showing that the main gain from the hybrid is not a uniform reduction at every resonance. The sharp feature near 1.5 GHz corresponds to the accelerating TM_{020} mode and is distinguished from the HOM comparison. For the 0.5 GeV LUTF storage ring, the black threshold represents operation without harmonic-cavity bunch lengthening, while the red and blue curves represent optimal and threefold bunch lengthening. Several hybrid HOM features exceed the black curve; the higher bunch-lengthening thresholds give a more favorable operating comparison.

The transverse spectra in Fig. 10(b) likewise depend on the assumed stabilization system. Resonances near 1 and 2 GHz are lower for ferrite-containing loads than for the pure-SiC case, while a prominent feature remains near 2.6 GHz for all three designs. Several peaks exceed the solid horizontal thresholds, which represent natural damping, but lie below the higher dash-dotted thresholds associated with active feedback damping. The absorber therefore reduces the impedance burden on the beam

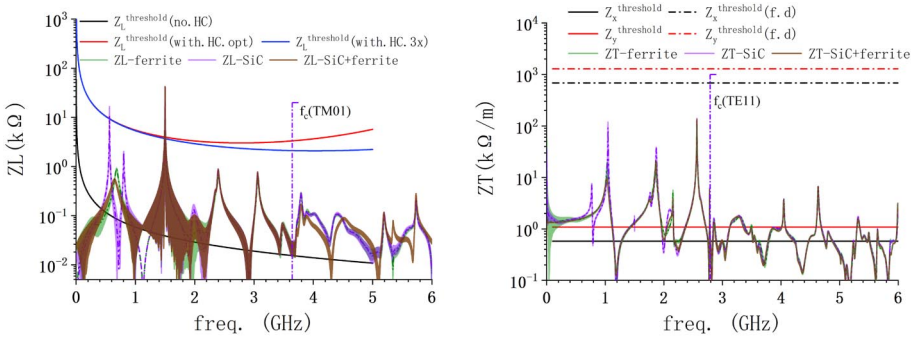


FIG. 10. Broadband (a) longitudinal and (b) transverse wakefield impedances for ferrite (green), SiC (purple), and hybrid (brown) absorbers. Longitudinal thresholds correspond to no harmonic cavity (black), optimal harmonic-cavity bunch lengthening (red), and threefold bunch lengthening (blue). Transverse x/y thresholds are black/red: solid lines denote natural damping and dash-dotted lines denote feedback damping ("f. d"). Vertical markers identify the TM_{01} and TE_{11} beam-pipe cutoffs. HC denotes harmonic cavity.

stabilization system without making the feedback assumption irrelevant. The modal and wakefield results together favor the hybrid as a broadband damping arrangement, with the beam-stability assessment tied to the bunch lengthening and feedback conditions represented in the figure.

The cutoff markers indicate when the circular beam pipe can support propagating TM_{01} and TE_{11} waves. For vacuum radius b_p, $f_{c,TM01} = 2.405c/(2\pi b_p)$ and $f_{c,TE11} = 1.841c/(2\pi b_p)$. Below the relevant cutoff, the corresponding field decays along the pipe and damping relies on other accessible channels, including the local absorber. Above cutoff, power can propagate along the pipe, with extraction governed by its termination. The markers consequently help interpret changes in the spectral environment. They are not instability thresholds or multiplicative corrections to R^*_{sh}, and they are not used as lower limits when integrating the total HOM loss: modes below cutoff can still contribute to beam-induced heating.

C. Beam-induced power and material loss partitioning

The reference beam has average current $I_0 = 1.0$ A, bunch charge $q = 2.0$ nC, and rms bunch length $\sigma_z = 10$ mm. For a Gaussian bunch, the longitudinal loss factor is obtained by weighting $\mathrm{Re}Z_\parallel(\omega)$ with $e^{-\omega^2\sigma_z^2/c^2}$. The cumulative quantity is $k(F) = (1/\pi)\int_0^{2\pi F} \mathrm{Re}Z_\parallel(\omega)e^{-\omega^2\sigma_z^2/c^2}d\omega$. Thus, F is the upper integration frequency, while σ_z sets the spectral weighting. The bunch loses energy q^2k and the corresponding broadband average power is qI_0k.

Figure 11 rises in steps at the stronger resonances and more gradually where the impedance contribution is distributed over frequency. The cumulative value is about

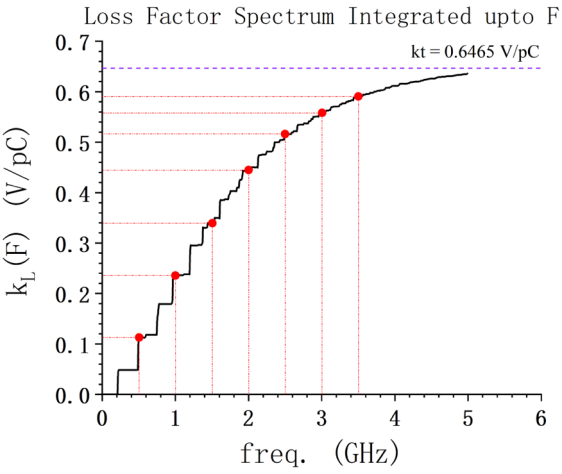


FIG. 11. Cumulative longitudinal loss factor $k(F)$, with Gaussian bunch-spectrum weighting and upper integration frequency F. The dashed line indicates $k_{tot} = 0.6465$ V/pC; markers illustrate the accumulated loss at selected frequencies.

0.45 V/pC at 2 GHz and approaches the indicated total of 0.6465 V/pC at higher frequencies. The continued increase beyond 2 GHz shows that the upper part of the spectrum remains relevant to the heat load, even when individual high-frequency peaks are modest. This is the power-budget motivation for including SiC: reducing the low-frequency impedance alone does not eliminate the accumulated loss from higher-frequency modes. The total curve includes the accelerating-mode contribution, which is separated when constructing an HOM-only budget.

$$P_{broad}(> f_c) = [k_{tot} - k(f_c)]qI_0 \tag{16}$$

In Eq. (16), f_c denotes a chosen frequency partition. For total HOM power, the accelerating mode is subtracted explicitly instead of discarding all frequencies below its resonance. With the voltage and R/Q convention of Sec. II, its Gaussian-bunch loss factor is $k_0 = (\omega_0/4)(R/Q)_0 e^{-\omega_0^2\sigma_z^2/c^2}$, or equivalently $k_0 = [\omega_0 R^*_{sh,0}/(2Q_{L,0})]e^{-\omega_0^2\sigma_z^2/c^2}$. The broadband HOM power is then $(k_{tot} - k_0)qI_0$. Retaining the low-frequency HOMs is particularly relevant for this cavity because TM_{010} lies below the operating TM_{020} frequency.

Frequency-resolved field losses explain how this power is shared between the two materials. At an incident normalization of 0.5 W, the 0.5–1.5 GHz maps in Fig. 12 show relatively strong deposition along the outer ferrite region. Near 2 GHz, the inner SiC region becomes more active; by 2.5–4 GHz, pronounced loss bands are visible within SiC. The transition follows the combination of frequency-dependent constitutive loss and the changing internal field pattern. It shifts a substantial part of the higher-frequency dissipation into the material with higher thermal conductivity, providing the electromagnetic basis for the subsequent thermal comparison.

The volume-integrated SiC fraction in Fig. 13 gives a more direct measure than the contour colors alone. It is small below 1 GHz, increases through the 1.5–2 GHz interval, and reaches approximately 0.8 near 2.5–3 GHz. It then decreases modestly around 3.5 GHz while remaining substantial at 4 GHz. This nonmonotonic behavior shows that the materials share the load over overlapping frequency ranges, rather than divide it at a sharp 2 GHz boundary. Meanwhile, the total efficiency is high around 1.5–2 GHz and remains appreciable as the SiC fraction grows. Redistribution therefore occurs while the absorber continues to admit and dissipate rf power.

For each excitation frequency, the material fraction is obtained from $P_{SiC}/(P_{SiC} + P_{ferrite})$, with each power defined by its volume integral. A thermal budget additionally weights these fractions by the beam spectrum and the accelerating-mode leakage. The normalized maps establish spatial patterns and relative participation; their local maxima are not directly the operating power density



FIG. 12. Hybrid-absorber volumetric power-loss density at (a)–(h) 0.5, 1.0, 1.5, 2.0, 2.5, 3.0, 3.5, and 4.0 GHz, normalized to 0.5 W incident power. All panels use the common nonlinear color scale in $\mathrm{W/m^3}$; individual maxima are labeled in $\mathrm{kW/m^3}$. The inner region is SiC, and the outer region is ferrite.

of the kilowatt load case. This distinction allows the same electromagnetic model to inform both broadband damping and heat-source allocation without equating a frequency band exclusively with one material.

A periodic bunch train samples the impedance at discrete revolution harmonics. Write the real current as $i(t) = I_0 + 2\mathrm{Re}\sum_{n\geq 1} I_n \exp(jn\omega_{\mathrm{rev}}t)$, where I_n includes the Gaussian bunch form factor and the phases of the occupied buckets. The average HOM power is

$$P_{\mathrm{HOM,train}} = 2\sum_{n\geq 1}|I_n|^2 \mathrm{Re}\, Z_{\mathrm{HOM}}(n\omega_{\mathrm{rev}}). \tag{17}$$

The factor 2 accounts for the positive- and negative-frequency components of the real current. For an isolated longitudinal resonance exactly on a beam harmonic, the contribution is $2|I_n|^2 R^*_{\mathrm{sh},\|}$. Close to resonance, the impedance is approximately $R^*_{\mathrm{sh},\|}/[1 + 4Q_L^2((n\omega_{\mathrm{rev}} - \omega_m)/\omega_m)^2]$. Thus, both the line width and the occupied-harmonic spectrum control resonant heating. When a broadband estimate and a resonant correction are combined, the correction is the train-spectrum power of the selected modes minus their contribution already included in the broadband baseline.

The HOMs in Table II have widths $f_m/Q_{L,m}$ of approximately 18–54 MHz. A frequency displacement of ± 2 MHz is consequently small relative to these widths. For a single harmonic initially at line center, the Lorentzian expression gives a reduction of approximately 0.5%–4.7% at that displacement across this width range. This scale comparison explains why strongly damped modes are less sensitive to small resonance shifts than narrow high-Q modes. Total train-induced power nevertheless depends on how multiple revolution harmonics sample each resonance; the width estimate alone does not determine a maximum over all fill patterns.

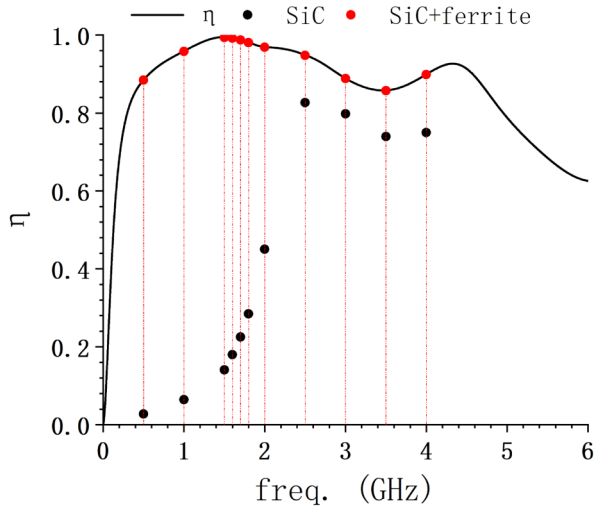


FIG. 13. Total absorption efficiency η (solid curve, with red frequency markers) and SiC share of absorbed power (black markers). The SiC fraction is $P_{\mathrm{SiC}}/(P_{\mathrm{SiC}} + P_{\mathrm{ferrite}})$, evaluated from material-volume loss integrals.

D. Thermomechanical response and design implications

The thermomechanical calculations compare both assemblies under a prescribed continuous-wave absorber

load of 2.65 kW. The adopted load budget consists of a 1.15 kW HOM contribution, formed from a 1.033 kW broadband estimate and a 0.117 kW allowance for train-induced variation, together with a 1.50 kW accelerating-mode leakage contribution. These values define the comparison case rather than a maximum over arbitrary beam fill patterns. The total is

$$P_{\mathrm{abs,case}} = P_{\mathrm{HOM,case}} + P_{\mathrm{leak,case}} = 1.15\ \mathrm{kW} + 1.50\ \mathrm{kW} = 2.65\ \mathrm{kW}. \tag{18}$$

The hybrid heat load is allocated as 1.80 kW in ferrite and 0.85 kW in SiC, whereas the pure-ferrite assembly absorbs the same 2.65 kW total. Both models connect the absorber pieces to water-cooled oxygen-free copper supports. Fixing the total power isolates the influence of material distribution and the associated thermal paths on temperature and stress. The leakage allocation corresponds to the displaced-geometry case at $P_c = 30$ kW described in Sec. II. It therefore probes a more demanding heat load than the 90.3 W leakage of the nominally aligned cavity.

The rf loss distribution supplies the volumetric heat source p_v to the steady-state conduction problem. The temperature field then provides the thermal strain in the structural calculation. For the linear isotropic material description used for this comparison, the governing relations are

$$-\nabla \cdot (k\nabla T) = p_v \tag{19}$$

$$\nabla \cdot \sigma = 0, \qquad \sigma = C : [\epsilon(u) - \alpha(T - T_{\mathrm{sf}})I]. \tag{20}$$

Here, C is the elastic stiffness tensor determined by E and ν, $\epsilon(u)$ is the small-strain tensor, I is the identity tensor, and T_{sf} is the stress-free reference temperature. The plotted thermal quantity is the rise $\Delta T = T - T_{\mathrm{ref}}$, where T_{ref} is the thermal reference. Conductivity controls the gradients needed to transport heat to the support, while constraints and differential expansion determine how that temperature field produces stress. This formulation is applied to the integrated geometry, so the interpretation includes the segmented material arrangement and support paths rather than an isolated uniform cylindrical absorber.

Figure 14 shows that the hybrid improves all three peak response metrics under the common heat load. Peak power density decreases from 31.1 to 29.4 W/cm^3, a 5.5% reduction, while peak temperature rise decreases from 97.0 to 79.9 K, a 17.1 K or 17.6% reduction. The improvement in temperature is larger than the reduction in the local heat-source maximum, consistent with a

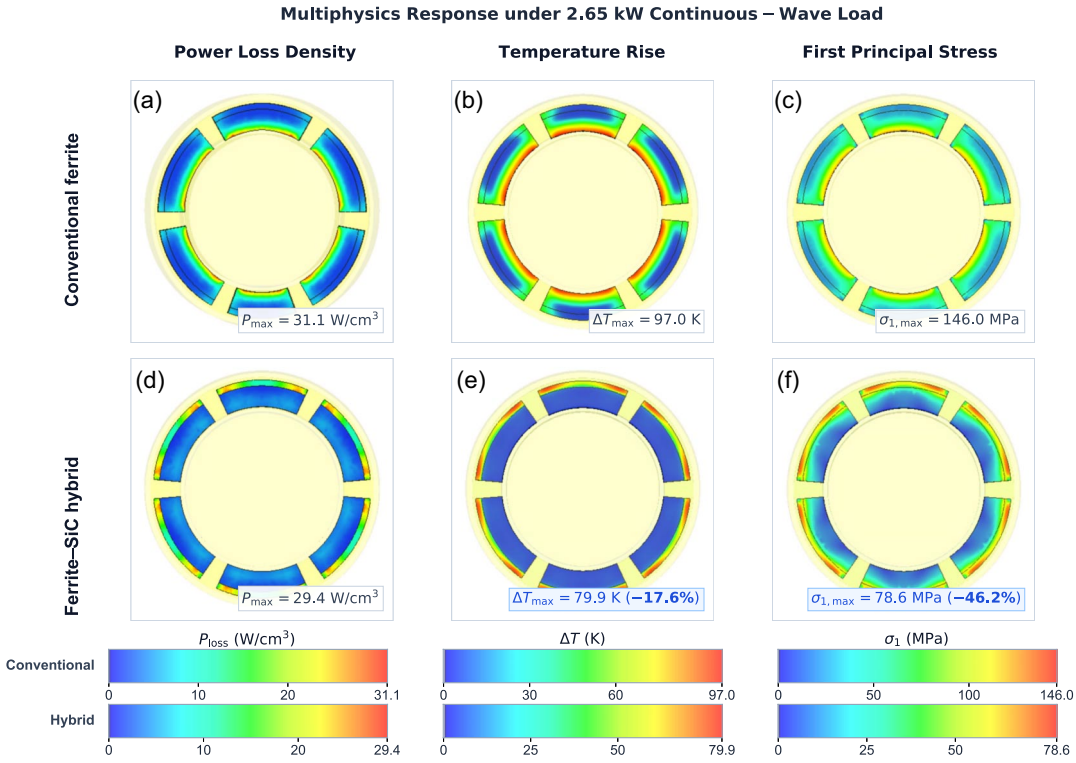


FIG. 14. Thermomechanical comparison at the same imposed 2.65 kW continuous-wave load. Upper row (a)–(c), pure ferrite; lower row (d)–(f), ferrite-SiC hybrid. Columns show power-loss density, temperature rise, and first principal stress σ_1. Their maxima are 31.1/29.4 W/cm^3, 97.0/79.9 K, and 146.0/78.6 MPa for pure ferrite/hybrid, respectively. Both stress maxima occur in ferrite. Separate color scales apply to the two rows. Panel (f) shows localized elevated stresses along segment edges.

change in heat transport as well as source localization. The higher conductivity of SiC provides a less resistive path for the fraction of power deposited there. Total absorbed power remains 2.65 kW, so these changes describe redistribution and thermal response at fixed integrated heating.

The maximum first principal stress σ_1 decreases from 146.0 MPa in the pure-ferrite assembly to 78.6 MPa in the hybrid, a reduction of 67.4 MPa or 46.2%. Both positive maxima occur in ferrite. The result therefore reflects relief of the tensile stress in the material common to both assemblies, rather than transfer of the reported maximum to a stronger SiC or copper region. Figure 14 also shows that the thermal and stress fields have different spatial patterns: stress depends on gradients, interfaces, and restraint, not only the hottest point. This explains the need to evaluate the coupled structural response after solving the thermal field.

A descriptive system-level ratio $K_{\sigma T} = \sigma_{1,\max}/\Delta T_{\max}$ decreases from 1.505 to 0.984 MPa/K, or by 34.6%. Scaling the pure-ferrite stress only by the peak-temperature-rise ratio would give $146.0 \times 79.9/97.0 = 120.3$ MPa, appreciably above the hybrid result of 78.6 MPa. The comparison indicates that the stress benefit exceeds uniform scaling with the temperature maximum. Redistribution of heating, altered conduction paths, and constrained expansion all provide plausible contributions. $K_{\sigma T}$ is a global response index, not a material constant: the stress and temperature maxima need not be co-located, and the 120.3 MPa value is a scaling reference rather than a separate structural simulation.

The stress pattern in Fig. 14(f) is concentrated along narrow segment-edge regions, while much of the displayed interior carries lower stress. Such a field loads a different population of potential fracture origins from an approximately uniform uniaxial tensile test. For brittle ceramics, specimen geometry, the stressed surface or volume, and flaw statistics affect the measured strength [19–21]. Three-point bending concentrates high tensile stress within a limited region, which helps explain why its measured strength can exceed the direct tensile result. Field-based reliability methods, including NASA CARES/LIFE, combine finite-element stress distributions with surface or volume flaw populations and multiaxial effects [22]. This provides a physical basis for interpreting localized thermal stress beyond a peak-only comparison.

The ferrite's measured three-point flexural strength $S_{\text{flex}} = 99.6$ MPa provides a useful test reference for comparing the two configurations [17]. The pure-ferrite peak gives $\sigma_{1,\max}/S_{\text{flex}} = 1.466$ and exceeds that reference by 46.4 MPa. The hybrid ratio is 0.789, placing its peak 21.0 MPa below the flexural value, with a nominal reference ratio $S_{\text{flex}}/\sigma_{1,\max} = 1.27$. The hybrid thus moves the calculated response from above to below the bending-test reference at the same imposed power. The direct tensile strength is 18.3 MPa, below both local stress maxima; the two strength measurements represent different stress distributions and are used here for comparative assessment. A component-specific allowable depends on the applicable field, flaw population, temperature, and strength statistics.

Taken together, the loss maps, temperature field, and stress response identify the advantage of the hybrid: part of the rf power is dissipated in a more conductive material, while the ferrite needed for lower-frequency damping experiences a smaller tensile concentration. The reduced stress is particularly relevant at the segment edges and interfaces where thermal expansion is restrained. Refinement of support compliance, joint geometry, and assembly gaps can target these regions without relying only on a reduction of total rf load. Prototype measurements of temperature distribution and joint behavior under continuous rf heating would test whether the modeled redistribution and restraint are representative of the assembled device.

VI. CONCLUSIONS AND OUTLOOK

A ferrite-SiC absorber has been developed numerically for a compact 1.5 GHz TM_{020}-mode cavity. The ordered transmission-line model explains why changing the material sequence alters input impedance, and the coaxial calculations favor SiC ahead of ferrite for avoiding strong absorption gaps over the studied band. Folding this path radially permits a six-sector absorber to be integrated near the accelerating-mode magnetic node. The full-wave parameter sweeps resolve the trade-offs among SiC dimension, slot height, and sector angle, providing a basis for selecting a compact single-layer arrangement rather than maximizing absorbing volume alone.

The integrated calculations connect this local absorption behavior to cavity performance. The six selected HOMs have $Q_{\text{ext}} \leq 150$, while the aligned accelerating mode has $Q_{\text{ext,leak}} = 1.20 \times 10^7$. Wakefield spectra show the benefit of ferrite-containing loads at lower frequencies and place the broadband response in the context of harmonic-cavity bunch lengthening and transverse feedback. Frequency-resolved loss maps and material integrals show substantial transfer of dissipation to SiC above the transition around 2 GHz, linking broadband electromagnetic response to heat-source allocation.

At the same imposed 2.65 kW continuous-wave absorber load, the hybrid reduces peak temperature rise by 17.6% and maximum first principal stress in ferrite by 46.2%. The stress reduction exceeds scaling with the temperature maximum alone, supporting the importance of the spatial thermal and mechanical response. These findings identify the hybrid as a route to accommodating residual accelerating-mode leakage alongside HOM heating in a compact cavity. Further development should connect the predicted segment and interface response to rf prototype measurements, so that geometry and thermal contact can be refined under representative operating conditions.

ACKNOWLEDGMENTS

This work was supported by Guangdong Basic and Applied Basic Research Foundation (Grant No. 2026A1515012618), Guangdong Basic and Applied Basic Research Foundation (Grant No. 2025A1515110437), and the Pre-research Project for the Ultra-fast and Transient Experimental Facility (Grant No. 2020-500356-83-01-128945).

DATA AVAILABILITY

The data that support the findings of this article are not publicly available upon publication because it is not technically feasible and/or the cost of preparing, depositing, and hosting the data would be prohibitive within the terms of this research project. The data are available from the authors upon reasonable request.

[1] A. Smygacheva, V. Korchuganov, and Y. Fomin, Coupled bunch instabilities in the storage rings, in *Proceedings of the 25th RussianParticle Accelerator Conference (RuPAC-2016), St. Petersburg, Russia,2016* (JACoW Publishing, Geneva, Switzerland, 2017), pp. 395–397, 10.18429/JACoW-RuPAC2016-WEPSB016.

[2] R. R. Lindberg, Theory of coupled-bunch longitudinal instabilities in a storage ring for arbitrary rf potentials, Phys. Rev. Accel. Beams **21**, 124402 (2018).

[3] P. Tavares, F. Cullinan, Å. Andersson, D. Olsson, and R. Svärd, Beam-based characterization of higher-order-mode driven coupled-bunch instabilities in a fourth-generation storage ring, Nucl. Instrum. Methods Phys. Res., Sect. A **1021**, 165945 (2022).

[4] H. Ego, J. Watanabe, S. Kimura, and K. Sato, Design of a HOM-damped RF cavity for the SPring-8-II storage ring, in *Proceedings of the11th Annual Meeting of Particle Accelerator Society of Japan (PASJ2014), Aomori, Japan, 2014* (Particle Accelerator Society of Japan, Tokyo, Japan, 2014), paper MOOL14, pp. 60–64.

[5] H. Ego, H. Tanaka, T. Inagaki, T. Ohshima, H. Yamaguchi, T. Tomai, T. Asaka, and N. Nishimori, Compact HOM-damping structure of a beam-accelerating TM020 mode RF cavity, Nucl. Instrum. Methods Phys. Res., Sect. A **1064**, 169418 (2024).

[6] T. Yamaguchi, N. Yamamoto, D. Naito, T. Takahashi, and S. Sakanaka, Design and low-power measurement of 1.5 GHz TM020-type harmonic cavity for KEK future synchrotron light source, Nucl. Instrum. Methods Phys. Res., Sect. A **1053**, 168362 (2023).

[7] J. M. Byrd, S. De Santis, J. Jacob, and V. Serriere, Transient beam loading effects in harmonic RF systems for light sources, Phys. Rev. ST Accel. Beams **5**, 092001 (2002).

[8] X. Hao, J. Zhu, X. Li, Z. Liu, C. Zhang, W. Long, S. Chen, Y. Liu, S. Liu, and B. Wu, A study of the electromagnetic fields leakage in TM020 mode HOM-damped cavity, Nucl. Eng. Technol. **57**, 103717 (2025).

[9] Z. Li, K. Ye, L. Yang, Y. Zhang, X. Zhou, X. Yang, and X. Hao, Electromagnetic field compensation to attenuate energy leakage in TM020 mode damped cavity, Nucl. Eng. Technol. **57**, 103256 (2025).

[10] A. D'Elia *et al.*, HarmonLip 2024 (2024), https://indico.esrf.fr/event/122/contributions/668/attachments/393/784/HarmonLip2024deliav2.pptx.

[11] W. Xu, Z. A. Conway, E. Daly, J. Guo, K. Hernandez, D. Holmes, R. A. Rimmer, F. Severino, K. Smith, D. Weiss, and A. Zaltsman, High-power test results for a cylindrical-shell silicon carbide higher-order-mode damper, Phys. Rev. Accel. Beams **27**, 031601 (2024).

[12] H. Hahn, E. M. Choi, and L. Hammons, Ferrite HOM absorber for the RHIC ERL, Technical Report, Brookhaven National Laboratory (BNL), Upton NY (United States), 2008, Relativistic Heavy Ion Collider (RHIC), https://www.osti.gov/biblio/1061919.

[13] T. Yamaguchi, S. Sakanaka, N. Yamamoto, D. Naito, T. Takahashi *et al.*, Optimization of the parasitic-mode damping on the 1.5 GHz TM020-type harmonic cavity, in *Proceedings of the 12th International ParticleAccelerator Conference (IPAC'21), Campinas, SP, Brazil, 2021* (JACoWPublishing, Geneva, Switzerland, 2021), pp. 1064–1067, 10.18429/JACoW-IPAC2021-MOPAB343.

[14] Y. Takeuchi, T. Abe, T. Kageyama, and H. Sakai, RF dielectric properties of SiC ceramics and their application to design of HOM absorbers, in *Proceedings of the 2005 Particle Accelerator Conference(PAC 2005), Knoxville, Tennessee, USA, 2005* (IEEE, Piscataway, NJ, 2005), pp. 1195–1197, 10.1109/PAC.2005.1590705.

[15] CoorsTek Inc., Advanced silicon carbide for critical components, in *Silicon Carbides Brochure* (CoorsTek Inc., Golden, Colorado, USA, 2017), https://www.coorstek.com/en/materials/silicon-carbide/.

[16] J. L. Snoek, Dispersion and absorption in magnetic ferrites at frequencies above one Mc/s, Physica **14**, 207 (1948).

[17] Standard Testing, Test Report No. STD-20200714-039 N (2020), p. 2 of 3. Ferrite tensile strength 18.3 MPa; no yielding observed in tension; tensile modulus 110 GPa; three-point flexural strength 99.6 MPa; compressive strength 274 MPa; Poisson ratio 0.23. Test environment 21–22 °C, 53–54% RH. Reported methods: GB/T 1040.2-2006 (reference method for tensile strength), GB/T 23805-2009, GB/T 6569-2006, and GB/T 8489-2006..

[18] Standard Testing, Test Report No.: STD-20190903-032 N-3, Technical Report, Standard Testing, 2019.

[19] ASTM International, ASTM C1161-18(2023) Standard Test Method for Flexural Strength of Advanced Ceramics at Ambient Temperature, Secs. 4.3–4.6, https://store.astm.org/c1161-18r23.html.

[20] G. D. Quinn, Weibull effective volumes and surfaces for cylindrical rods loaded in flexure, J. Am. Ceram. Soc. **86**, 475 (2003).

[21] ASTM International, ASTM C1239-26, Standard practice for reporting uniaxial strength data and estimating Weibull distribution parameters for advanced ceramics (2026), https://store.astm.org/c1239-26.html.

[22] N. N. Nemeth, L. M. Powers, L. A. Janosik, and J. P. Gyekenyesi, CARES/LIFE ceramics analysis and reliability evaluation of structures life prediction program, NASA/TM-2003-106316 (2003), https://ntrs.nasa.gov/citations/20030014949.